BNL-225461-2024-JAAM

GRP-COEE-30

Ligand-channel-enabled ultrafast Li-ion conduction

D. Lu, E. Hu

To be published in "Nature"

February 2024

Chemistry Department

Brookhaven National Laboratory

U.S. Department of Energy

USDOE Office of Energy Efficiency and Renewable Energy (EERE), Office of Sustainable Transportation. Vehicle Technologies Office (VTO)

Notice: This manuscript has been authored by employees of Brookhaven Science Associates, LLC under Contract No.DE-SC0012704 with the U.S. Department of Energy. The publisher by accepting the manuscript for publication acknowledges that the United States Government retains a non-exclusive, paid-up, irrevocable, world-wide license to publish or reproduce the published form of this manuscript, or allow others to do so, for United States Government purposes.

DISCLAIMER

This report was prepared as an account of work sponsored by an agency of the United States Government. Neither the United States Government nor any agency thereof, nor any of their employees, nor any of their contractors, subcontractors, or their employees, makes any warranty, express or implied, or assumes any legal liability or responsibility for the accuracy, completeness, or any third party's use or the results of such use of any information, apparatus, product, or process disclosed, or represents that its use would not infringe privately owned rights. Reference herein to any specific commercial product, process, or service by trade name, trademark, manufacturer, or otherwise, does not necessarily constitute or imply its endorsement, recommendation, or favoring by the United States Government or any agency thereof or its contractors or subcontractors. The views and opinions of authors expressed herein do not necessarily state or reflect those of the United States Government or any agency thereof.

Ligand channel enabled ultra-fast Li-ion conduction

Di Lu[1]†, Ruhong Li[1]†, Muhammad Mominur Rahman[2], Ling Lv[1], Sheng Yang[3], Yiqiang Huang[1], Chuangchao Sun[1], Shuoqing Zhang[1], Haikuo Zhang[1], Junbo Zhang[1], Xuezhang Xiao[1], Tao Deng[4], Liwu Fan[3], Lixin Chen[1,5], Enyuan Hu[2,*] Chunsheng Wang[4,*], Xiulin Fan[1,*]

[1]State Key Laboratory of Silicon and Advanced Semiconductor Materials, School of Materials Science and Engineering, Zhejiang University; Hangzhou 310027, China.

[2]Chemistry Division, Brookhaven National Laboratory; Upton, New York, United States.

[3]State Key Laboratory of Clean Energy Utilization, School of Energy Engineering, Zhejiang University; Hangzhou, 310027, China

[4]Department of Chemical and Biomolecular Engineering, University of Maryland, College Park; MD 20742, USA.

[5]Key Laboratory of Advanced Materials and Applications for Batteries of Zhejiang Province; Hangzhou 310013, China

*Corresponding author. Email: xlfan@zju.edu.cn; cswang@umd.edu; enhu@bnl.gov

†These authors contributed equally to this work.

Abstract

Li-ion batteries (LIBs) for electric vehicles and aviation demand high energy density, fast charging, and wide operating temperature, which is impossible because it requires electrolytes to have high ionic conductivity, low solvation energy, low melting point, and form anion-derived interphase simultaneously. Herein, we propose the guidelines for high-performance electrolytes with low-solvation energy and high ionic conductivity even at ultra-low temperatures by using small-sized solvents. The tiny solvent in the secondary solvation sheath pulls out the Li^+ in the primary solvation sheath to form a fast ion conduction ligand channel and promise rapid Li^+ transport, while the small-sized solvent with low-solvation energy also allows the anion to enter the first Li^+ solvation shell to form inorganic-rich interphase. The electrolyte design concept is demonstrated by using a low-solvation and small-sized fluoroacetonitrile (FAN) solvent. The electrolyte of 1.3 M lithium bis(fluorosulfonyl)imide (LiFSI) in FAN exhibits ultra-high ionic conductivity of 40.3 mS cm^{-1} at 25 °C and 11.9 mS cm^{-1} even at -70 °C, which is over 4 orders of magnitude larger than that of traditional electrolytes. Our designed electrolyte enables high voltage 4.5 V graphite||$LiNi_{0.8}Mn_{0.1}Co_{0.1}O_2$ full cells to deliver ultra-stable cycling at 6 C at 25 °C and 4.5 V graphite||$LiNi_{0.8}Mn_{0.1}Co_{0.1}O_2$ pouch cells (1.2 Ah, 2.85 mAh cm^{-2}) to achieve high reversibility (0.62 Ah) when charged and discharged at -65 °C. The electrolyte design based upon ligand channel facilitated mechanism with small-sized solvents enables LIBs to simultaneously achieve high energy density, fast charging, and wide-temperature operation, which is unattainable for the current electrolyte design but is

highly desired for extreme LIBs. This elucidated mechanism is generalizable and can be expanded to encompass all metal-ion battery electrolyte designs.

Keywords: Electrolyte, fluoroacetonitrile, fast-charging, low-temperature, lithium-ion battery

Introduction

The proliferation of battery applications from portable electronics to electric vehicles, grid storage, space/subsea exploration, and electrified aviation[1,2], has led to a significant surge in demand for high-performance Li-ion batteries (LIBs). Such market expansion requires LIBs to have high energy density and operate at high rates and low temperatures without compromising the cycle life[3-5], requiring the electrolytes to form LiF-rich interphase on both graphite anode and high-voltage cathode, to have a high ionic conductivity, low solvation energy, and low freezing temperatures[6], which is impossible for current electrolytes.

The electrolyte properties, including ionic conductivity, solvation/desolvation behaviors and interphase chemistry, are controlled by the interactions between solvents, Li^+ cations and salt anions[5,7]. The ethylene carbonate (EC)-based electrolytes have a high ionic conductivity (9-10 mS cm^{-1} at 25 °C) and form organic-inorganic solid electrolyte interphase (SEI) on graphite anodes due to the strong interactions of Li^+-solvents, which support the reversibility of graphite-based LIBs under mild working conditions[8]. However, the high desolvation energy and organic-rich SEI increase the interfacial resistance, especially at low temperatures. The high solidification

temperature of EC-based electrolytes further limits the low-temperature performance[9]. High-concentration electrolytes (HCE), localized high-concentration electrolytes (LHCE) and weakly solvating electrolyte (WSE) address the interfacial issue by forming anion-derived SEI[10-13], yet they invariantly have low ionic conductivities (around 1 mS cm^{-1}) due to poor lithium salt dissociation, which limits the charging rates and power densities[13,14]. It is impossible for the electrolyte to simultaneously have high ionic conductivity and form LiF-rich SEI, based on the current electrolyte design principle.

Li^+ in liquid electrolytes with different salt concentrations can transport either through a vehicular (Fig. 1a) or structural transport mechanism (Fig. 1b), or a combination of both[15,16]. Pure structural diffusion can only be observed in the single-ion conducting solid-state electrolytes[17], in which the energy barrier of Li^+ hopping controls the diffusion kinetics[18]. For the case of organic liquid electrolytes, both vehicular and structural mechanisms are often present, depending on the salt concentration and Li^+ solvation structure[19]. In traditional liquid (dilute) electrolytes, vehicular transport is the dominant ionic conduction manner, in which Li^+ moves with its bulky solvation sheath[20,21]. However, in HCE, Li^+ diffusion occurs mainly through hopping to solvents and anions by sequential shifts between various possible configurations of multidentate ligation *via* structural diffusion mechanism[22,23]. The high energy barrier in HCE is primarily induced by stiff percolated interconnected ion with solvent/anion networks and close-knit coordination[24,25]. In both the vehicular and structural mechanisms, only the Li^+ solvation energy in the first solvation sheath is

considered due to the shielding effect from the large-sized solvents and anions in the primary solvation sheath. Therefore, weak bonding between Li^+ and solvents is desirable for allowing anion to enter the Li^+ primary solvation shell. However, weak-solvation significantly suppresses the full dissociation of Li-salts, resulting in the decrease of Li-ion conductivity. How to keep the benefit of weak bonding between Li^+ and anion/solvents while achieving a fast Li^+ transport in the liquid electrolyte remains an unsolved challenge for current organic electrolyte design.

Here, we report a ligand channel mechanism, in which the Li^+ interacts with the small-sized solvent molecules in both the inner- and outer-sheath forming a continuous Li^+ transporting "ligands" channel, which significantly reduces Li^+ transport energy barrier and facilitates ion diffusion in the electrolyte (Fig. 1c). In addition, the small-sized solvent in the first solvation shell also enables anion to bond with Li^+ to form anion-derived inorganic SEI. We used a novel solvent of fluoroacetonitrile (FAN) solvent with a low solvation energy of -4.42 eV and small shell volume of 255.60 $Å^3$ to demonstrate the "ligand channel facilitated mechanism". The new type of 1.3 M lithium bis(fluorosulfonyl)imide (LiFSI)/FAN electrolyte achieves ultra-high ionic conductivity (40.3 mS cm^{-1} at 25 °C, 11.9 mS cm^{-1} at -70 °C), and also enables to form LiF-Li_xN rich SEI, which is impossible for all reported low-temperature electrolytes[26-29]. The weak-solvation and small-sized FAN forms fast ligand Li-ion transport channel and allows FSI^- anion to enter the Li^+ primary solvation shell, promoting the formation of inorganic LiF-Li_xN interphase on graphite anode and NMC cathode through sequential decomposition of FSI^- and FAN to achieve high energy and high power

density. The 1.3 M LiFSI/FAN electrolyte enables graphite||$LiNi_{0.8}Mn_{0.1}Co_{0.1}O_2$ (NMC811) full cells to deliver reversible capacities of 208.1 mAh g^{-1} at 0.1 C and 184.8 mAh g^{-1} at 6 C and maintain 80% of capacity after 3000 cycles at 25 °C. Impressively, the FAN-based electrolyte allows 4.5 V graphite||NMC811 pouch cells (1.2 Ah) with high loading of 2.85 mAh cm^{-2} to maintain >60% of room temperature capacity and long cyclability at an ultra-low temperature of -65 °C. The ligand channel facilitated mechanism enables the low-temperature electrolyte (<-80 ºC) to simultaneously achieve high oxidation voltage (>4.5 V) and high ionic conductivity (>40 mS cm^{-1}), which is impossible for the electrolytes designed from vehicular or structural mechanism. The ligand channel transport mechanism is universal and suitable to design electrolytes for other metal-ion batteries.

Results and Discussion

Small-sized solvent with weak solvation energy and high Li-ion conductivity

The dissociation of lithium salt is strongly influenced by the interaction between the solvent and salt, as well as the interaction between the cation and anion. Typically, a high degree of dissociation is observed when there is a strong solvent-salt interaction and a weak cation-anion interaction. This behavior is positively correlated with high solvation energy[12,30]. The dissociation of lithium salt in the salt-in-solvent regime leads to negligible Li^+-anions interactions, enabling high ionic conductivity and low Li^+ transference number[7]. To generate LiF-rich SEI that is favorable for low-temperature operation and fast-charging, the fluorinated anion needs to be positioned in the first

solvation shell[12,26,31]. Achieving this requires a solvent to have low solvation energy, while also being able to dissolve the salt and achieve high Li-ion conductivity. However, these requirements are self-contradictory and have yet to be fulfilled simultaneously in an electrolyte.

We screened solvents based on the solvation energy (E_{sol}) (Fig. 1d) and found 1,3-dioxolane (DOL), methyl difluoroacetate (MDFA), methyl 2,2-difluoro-2-(fluorosulfonyl)acetate (MDFSA) and dimethyldimethoxysilane (DMMS) have low solvation energy due to the weak interaction with Li^+, which are consistent with previous reports[11,26,32]. Among these solvents, trimethyl phosphate (TMP) and water (H_2O) exhibit the maximum solvation energy of -5.24 eV and -5.38 eV, respectively, owing to the strong coordination with Li^+[33,34]. Despite having same solvation energy, acetonitrile (AN, -4.65 eV)/tetrahydrofuran (THF, -4.65 eV) and FAN (-4.42 eV)/ethyl methyl carbonate (EMC, -4.42 eV) display notable disparity in lithium salt dissociation (Fig. S1a) and ionic conductivity (Fig. S1b), suggesting other parameters also play a critical role in the ionic conductivity in addition to solvation energy. To gain a better understanding of the reason behind the observed differences in conductivity, we revisited the Li-ion transport mechanism in liquid electrolytes.

We calculated the Li-ion conductivity (σ) using a rigorous approach that incorporated both vehicular and structural transport mechanisms, which include the solvation sheath volume [VN_s, in which V and N_s are the molecular volume of the solvent and the solvation number of Li^+, respectively, equations (1) and (2)] and Li^+ transport energy barrier [E_{trans}, free energy extracted from Ab Initio molecular dynamics

(AIMD) trajectory of the probability distribution of Li^+-solvent among various Li^+ complexes, equation (3)][35,36] for fast Li-ion chemistries among a variety of solvents (Table S1):

$$\sigma = \sum \frac{(Z)^2 F C}{6\pi\eta r_s} \quad (1)$$

$$r_s{}^3 = \frac{3VN_s}{4\pi} + r_c{}^3 \quad (2)$$

$$\sigma = \frac{A}{T} C \exp\left(-\frac{E_{trans}}{k_B T}\right) \quad (3)$$

where Z is the valence order, C is the molar concentration of diffused Li^+, F is Faraday's constant, η is the viscosity of electrolyte, r_s, and r_c are the Stokes radius of solvated Li^+ and the crystallographic radius of Li^+ (0.076 nm)[35], respectively. T is the absolute temperature, A and k_B are pre-exponential factor and Boltzmann constant, respectively. From equations (1) and (2), σ is negatively correlated with the Stokes radius of solvated Li^+ (r_s) and the volume of entire solvation sheaths (VN_s). In conventional liquid electrolytes, solvated structure of Li^+ usually contains four lumping solvent molecules, leading to the impeding Li^+ diffusion[37]. According to equation (3), low E_{trans} is required to achieve high ionic conductivity, whereas E_{trans} is high in HCE[12]. Therefore, the Li-ion conductivity increased with the decrease of Li^+ transport energy barrier (E_{trans}) and solvation sheaths volume (VN_s). As shown in Fig. 1e, three solvents, *id est*, H_2O (140.28 $Å^3$, 1.86 kJ mol^{-1}), AN (228.30 $Å^3$, 1.90 kJ mol^{-1}) and FAN (255.60 $Å^3$, 1.94 kJ mol^{-1}) in the light green area, stand out due to their ultra-small sheath volume and low Li^+ transport energy barrier, making them the most promising solvent candidates for the electrolyte with ultra-high ionic conductivity. These three small-sized solvents in the secondary solvation sheath can interact with inner Li^+ and regulate solvated structures

(Fig. S2) to form “ligands” channels (Fig. 1c), thus facilitating fast ion chemistries. For H_2O, the high solvation energy (Fig. 1d) and minimized solvent size allow it to fill the secondary sheath without anions[30], which precludes the formation of an effective and robust SEI in diluent aqueous electrolytes. Furthermore, the narrow electrochemical stability window of 1.23 V, defined by the “Pourbaix-limit”, also excludes the adoption of aqueous electrolytes in high-energy-density LIBs[38,39]. Similarly, the high solvation energy of AN tends to preclude the anions from participating in Li^+ solvated structures (Fig. 1d). The poor reduction stability and passivation capability of AN result in severe reactions with lithium metal and lithiated graphite (Fig. S3), thereby ruling out AN as a viable solvent in diluent electrolytes. Although high-concentration strategy could mitigate the side reactions of AN-based electrolyte, its low ionic conductivity (0.98 mS cm^{-1}, 25 °C) cannot support high-loading cells at extreme conditions[40,41]. Among the screened solvent candidates, only FAN satisfies electrolyte design criteria of low solvation energy, low Li^+ transport energy barrier, and small solvent size, thereby facilitating the formation of LiF-rich SEI and achieving high ionic conductivity through a fast conduction ligand channel.

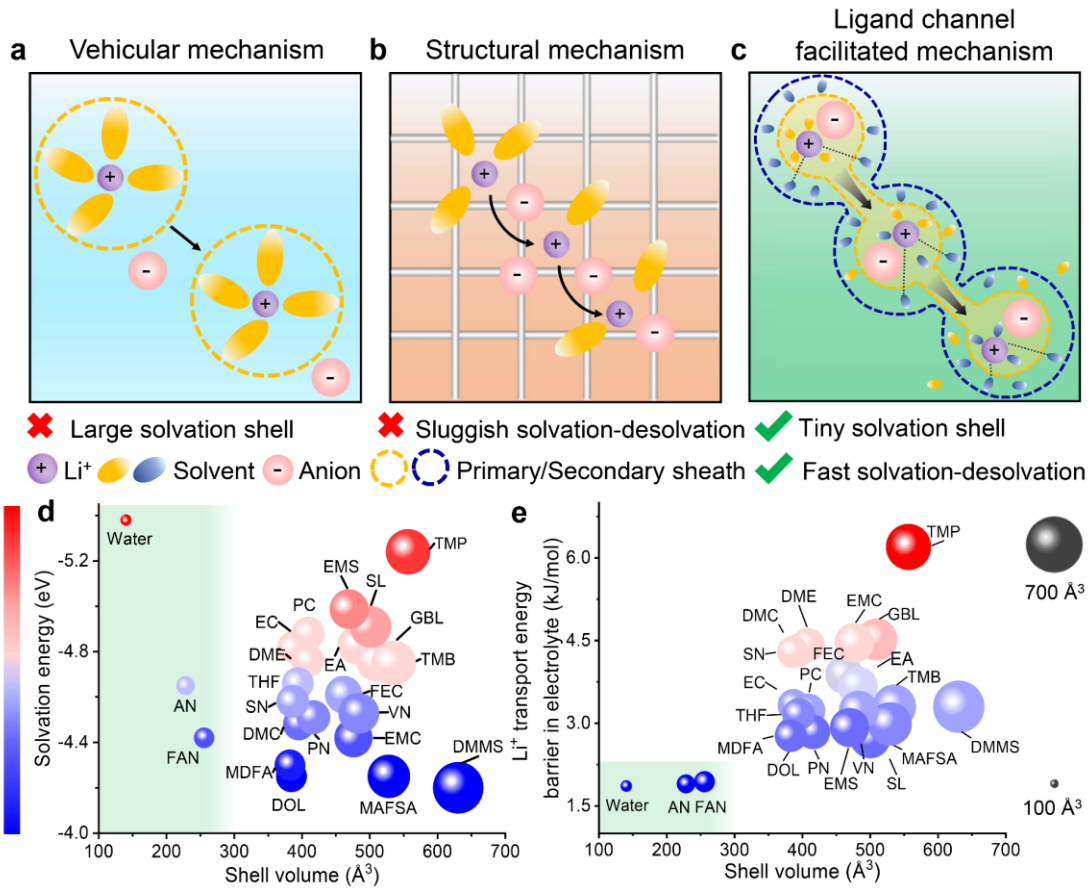

Fig. 1 | Electrolyte design and solvent screening strategies. a-c, Schematic illustrations of Li^+ transport behaviors with (**a**) Vehicular mechanism, (**b**) Structural mechanism and (**c**) Ligand channel facilitated mechanism. **d**, The solvation energy and solvation shell volume of solvents. **e**, The Li^+ transport energy barrier and solvation shell volume of solvents. The electrolyte using the solvents with small size, low solvation energy and Li^+ transport energy barrier can conduct Li^+ through ligand channel transport mechanism. The full name of every solvent can be found in the Table S1.

To demonstrate the electrolyte design criteria, we prepared 1.3 M LiFSI/FAN electrolyte, which achieves an ultra-high ionic conductivity of 40.3 mS cm^{-1} at 25 °C. Notably, the conductivity of 1.3 M LiFSI/FAN electrolyte is more than 4 times higher than that of typical traditional electrolytes, such as 1.0 M lithium hexafluorophosphate ($LiPF_6$)/EC-EMC electrolyte (9.0 mS cm^{-1}) (Fig. 2a and Fig. S4). High conductivity is also observed for FAN-based electrolyte with lithium bis(trifluoromethanesulfonyl)imide (LiTFSI) or $LiPF_6$ (Fig. 2a and Table S2). Fig. 2b

and Fig. S5 summarize the ionic conductivities of FAN-based electrolytes between 60 °C to -70 °C. The ion conductivities of six typical electrolytes, including (1) ionic liquid: 1.0 M LiFSI/N-methyl-N-propylpyrrolidinium bis(fluorosulfonyl)imide (Py_{13}-FSI), (2) HCE: 5.5 M LiFSI/dimethyl carbonate (DMC), (3) ether-based electrolyte: 1.0 M LiTFSI/DOL-1,2-dimethoxyethane (DME) (1:1, v/v), (4) traditional carbonate-based electrolyte: 1.0 M $LiPF_6$/EC-EMC (3:7, v/v) (5) LHCE: 1.2 M LiFSI/DMC-bis(2,2,2-trifluoroethyl) ether (BTFE) (1:2, n/n), and (6) $Li_{10}GeP_2S_3$ (LGPS), are also compared in Fig. 2b. It reveals that the ionic conductivity of traditional carbonate-based electrolyte exhibits an inflection point at -20 °C, with a low value of 2.0 mS cm^{-1}, which is followed by a rapid decline due to solidification of the electrolyte. In contrast, LiFSI/FAN electrolyte achieves the highest ionic conductivity of 11.9 mS cm^{-1} even at -70 °C, which is over 4 orders of magnitude greater than that of traditional carbonate-based electrolyte and surpasses the best-known reported electrolytes, including liquefied gas electrolyte (5.8 mS cm^{-1}, -60 °C)[28], ethyl acetate-based electrolyte (0.2 mS cm^{-1}, -70 °C)[29], fluorinated acetate-based electrolyte (0.01 mS cm^{-1}, -70 °C)[26] and fluorinated LHCE (1.1 mS cm^{-1}, -40 °C)[42]. Interestingly, the characteristic curves (log σ *vs.* 1/T) of 1.3 M LiFSI/FAN and 1.2 M LiTFSI/FAN are straight and parallel with each other (Fig. 2b), indicating ultra-low glass transition temperature of FAN-based electrolytes (Fig. S6b and Fig. S7). Additionally, Raman spectroscopy and intermolecular interaction matrix analysis clarify that significantly destructed H-bonds of FAN molecules lower the freezing point of FAN-based electrolyte (Fig. S8 and Fig. S9). Except for ionic conductivity, we also provide other transport parameters, *id est*,

transference number, self-diffusion coefficient and activity coefficient of FAN-based electrolyte to highlight fast ion conduction (Table S3).

Ligand channel facilitated mechanism

To understand the correlation between ligand channel facilitated mechanism and vehicular or structural mechanisms, we performed molecular dynamics (MD) simulations to investigate the molecular-scale solvation dynamics and the anion/solvent residence times around the Li^+ cations (Fig. 2c and Fig. S10). Our results show that the residence time of Li^+ in 1.3 M LiFSI/FAN electrolyte with the ligand channel facilitated mechanism is exceptionally short, while the Li^+ is frequently solvated by FAN molecules (~77.2 ps at 298 K) and FSI^- anions (~136.8 ps at 298 K) with ultra-fast hopping frequencies. Such a short time always results in a high Li^+ hopping frequency between the neighboring coordination sites and thereby high ionic conductivity[43]. This energetic Li^+ hopping is also verified by the decreased activation energy (0.85 eV, Fig. 2d) and the large spatial distribution of Li^+ ions around FAN solvent, as well as the long attracting distance of Li^+-FAN clusters (inset, Fig. 2d and Fig. S2). In traditional carbonate electrolytes, Li^+ diffusion occurs *via* vehicular mechanism, where Li^+ is carried along by the EC/EMC solvation sheaths with a longer coordination period (~198.5 ps at 298 K), owing to the strong affinity of solvated Li^+-inner EC/EMC molecules (Fig. S10a)[43,44]. With the increase of salt concentration, the Li^+ transport mechanism gradually transitions to a structural one, where Li^+ predominantly exchanges with FSI^- anions (~885.3 ps at 298 K, Fig. S10b).

As previously mentioned, an increase in salt concentration causes a shift in the Li^+

transport mechanism from vehicular to structural. The ionic conductivity initially increases and reaches a maximum value at around 1.0 M before decreasing thereafter (Fig. 2a). This suggests that the maximum ionic conductivity may be achieved during the transition from vehicular transport to structural transport. To better understand the fast Li^+ conduction mechanism in an electrolyte, we introduced the transport index (TI) as a new order parameter for quantifying Li^+ transport behavior, which represents the percentage of structural Li-ion transport in total Li-ion transport [equation (4), the details are shown in Fig. S11 and Supplementary Note 1]. In equation (4), N is the number of transport ions (Li^+), t_V is the time for Li^+ transport without solvent/anion exchange, t_S is the time for Li^+ transport accompanied by solvent/anion hopping. It is worth noting that the sum of t_V and t_S equals the total simulation time. $\Delta r_{i,j}$ and $\Delta r_{i,k}$ are the displacement of Li^+ that obey different types of ion motion mechanisms in a given time interval.

$$TI = \frac{S}{V+S} = \frac{1}{N}\sum_{i=1}^{N}\left(\frac{\sum_{r=0}^{t_S}\Delta r_{i,k}{}^2}{\sum_{j=0}^{t_V}\Delta r_{i,j}{}^2+\sum_{k=0}^{t_S}\Delta r_{i,k}{}^2}\right) \quad (4)$$

At TI = 0 (ideal dilute liquid electrolytes), the ion transport occurs *via* the vehicular mechanism. At TI = 1 (solid-state electrolyte), the Li^+ percolation with structural mechanism contributes to the integral Li^+ motion (Fig. S12). By clarifying the two parameters of ionic conductivity and TI in liquid electrolyte, the ion transport mode can be clearly revealed at molecular scale. For the standout electrolytes with a ligand channel facilitated mechanism, the maximum ionic conductivity is achieved when TI is located at around 0.5 (Fig. S13), and vice versa, which suggests a unique and ultra-fast

ion transport behavior that is different from vehicular/structural ones. As shown in Fig. 2a, 2e and Fig. S11, FAN-based electrolyte with a concentration of 1.3 M and TI value of ~0.5 presents the fastest ion translation property, far exceeding any other electrolytes. It is noteworthy that TI can be considered as a direct and effective means to design ideal electrolytes with superionic behavior.

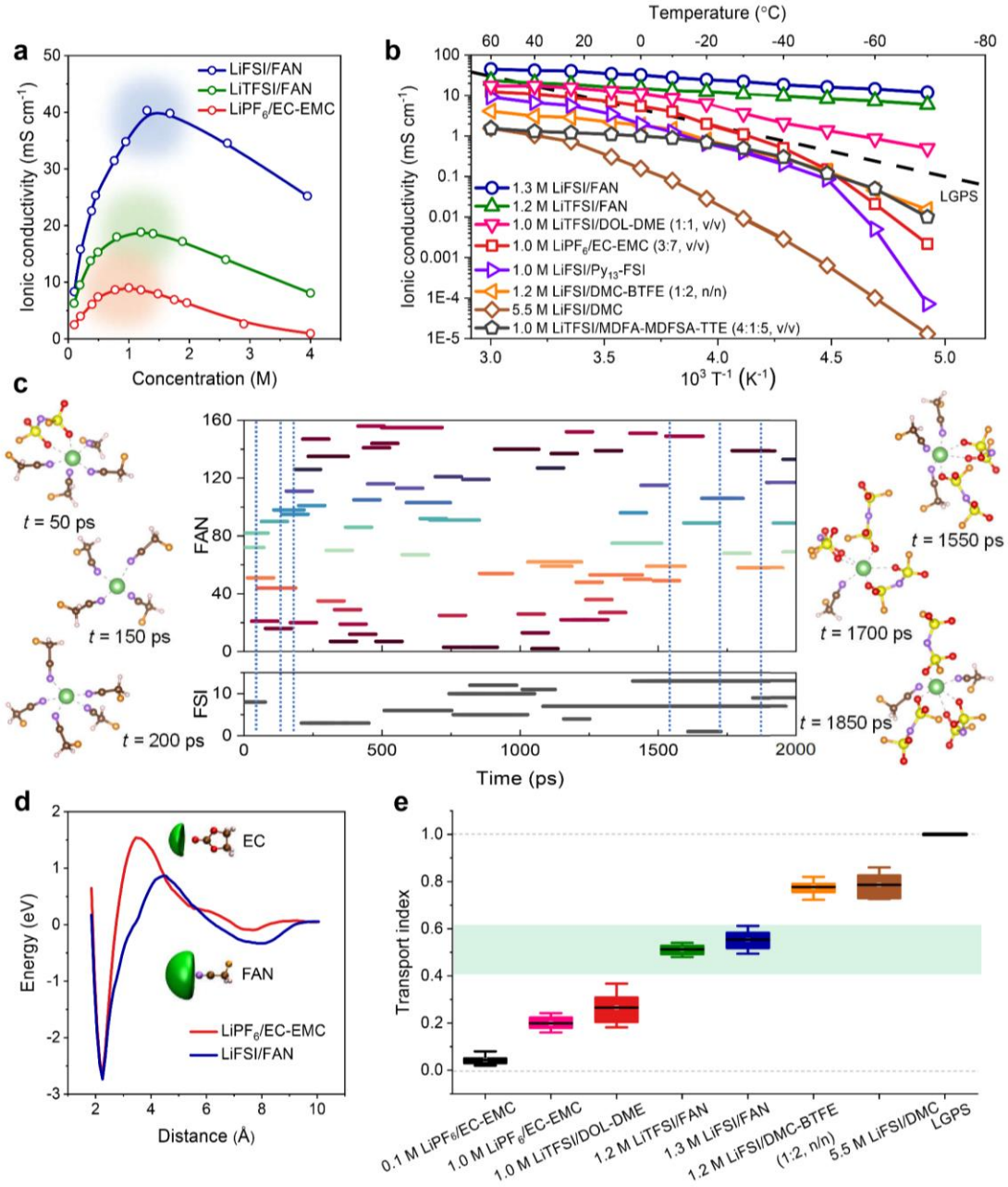

Fig. 2 | Physical properties and ion transport mechanism of FAN-based electrolyte. **a**, Ionic conductivities of EC/EMC-based and FAN-based electrolytes with different concentrations. **b**, Ionic conductivities of liquid and solid-state electrolytes from 60 °C

to -70 °C. **c**, Evolution of Li-ion solvation environment in 1.3 M LiFSI/FAN electrolyte from MD simulations at 298 K (the vertical axis represents serial number of different solvents or anions coordinated with the investigated Li^+ in the simulation time of 2000 ps). The horizontal short lines in the figure denote residence time of N(FAN) within 3.0 Å and O(FSI^-) within 3.0 Å of Li^+. The representative Li^+ solvation structures corresponding to different residence time indicated by vertical dash lines in the figure are also shown (t = 50 ps, 150 ps, 200 ps, 1550 ps, 1700 ps, 1850 ps. green: Li atom, red: O atom, yellow: S atom, purple: N atom, orange: F atom, tan: C atom, white: H atom). **d**, Variation of energy barrier of Li^+ hopping in different electrolytes (Inset: spatial distribution function of Li^+ ions around FAN and EC solvents). **e**, Transport indexes (TI) of different electrolytes. The error bars represent maximum and minimum values of TI. The mean values of TI are marked with black lines.

Solvation sheath structure of 1.3 M LiFSI/FAN electrolyte

NMR spectroscopy and MD simulations were utilized to unveil the solvation structure of 1.3 M LiFSI/FAN electrolyte. The downfield shift from -2.84 ppm to -2.61 ppm suggests a decreased shielding effect of FAN on Li^+ due to the strong electron-withdrawing capability by the substituting F atom (Fig. 3a), resulting in a weakened Li^+-N_{FAN} interaction and an increase of the Li^+-FSI^- interaction within the solvation sheath. This variation is consistent with the increase in the minimum electrostatic potential of FAN molecule (*vs.* AN molecule) (Fig. S14). According to the hotmaps of Li^+ solvation sheath in FAN and AN-based electrolytes (Fig. 3b and Fig. S15), the dominant solvation configurations of 1.3 M LiFSI/FAN and 1.3 M LiFSI/AN electrolytes are Li^+-3FAN-$2FSI^-$ and Li^+-4AN, respectively. As presented in the radial distribution function (RDF) and coordination number [n (r)] (Fig. 3c), the intensities of Li-N_{AN} and Li-$O_{FSI(FAN)}$ peaks are much stronger than those of Li-N_{FAN} and Li-$O_{FSI(AN)}$ peaks (around 2.1 Å). These results demonstrate the strong bonding of Li^+-FSI^- and weak coordination of Li^+-FAN in FAN-based electrolyte, which ensures the formation of the anion-derived interphase.

Similar to the classical case of "EC-propylene carbonate (PC) disparity"[37], the minuscule structural variation between AN and FAN caused by a single F atom leads to two totally distinct interphase behaviors: the continuously irreversible reduction of AN-based electrolyte at ~0.5 V, as opposed to the reversible Li^+ interaction/deintercalation enabled by FAN-based electrolyte at ~0.1 V (Fig. 3d). In the lithiation process of graphite, the Li^+ tends to get rid of partially solvated solvent molecules so that the energy barrier for solvent co-intercalation is minimized[37]. The competing interactions of solvent and anion with Li^+, quantified as the solvation energy, determine the desolvation processes (Fig. 3e and 3f). The solvation energies of FAN are always smaller than FSI^- ($\Delta E_{Li^+\text{-}FSI^-\text{-}3FAN}$ = 0.182 eV, $\Delta E_{Li^+\text{-}FSI^-\text{-}4FAN}$ = 0.095 eV, Fig. 3e), indicating that FAN molecule is prone to leaving the primary Li^+ solvation sheath during the desolvation process. The partially desolvated Li^+ containing FSI^- would then undergo the reductive decomposition reaction on the graphite surface to form a protective anion-derived SEI, facilitating the rapid Li^+ transfer and promising long cycle life of cells. In contrast, the solvation energies of AN are larger than FSI^- in dilute electrolytes ($\Delta E_{Li^+\text{-}FSI^-\text{-}3AN}$ = -0.130 eV, $\Delta E_{Li^+\text{-}FSI^-\text{-}4AN}$ = -0.113 eV, Fig. 3f), suggesting that it is more difficult for the Li^+ solvation sheath to lose AN than to lose FSI^-. Hence, the anion-free solvation structure of $Li^+(AN)_x$ is more likely to co-intercalate into graphite in AN-based electrolyte (Fig. 3d and Fig. S16). Such co-intercalation would lead to the generation of abundant gases and/or organic phases by solvent reductions, resulting in the exfoliation of the graphite. Furthermore, the optimized solvation structures of FAN and AN-based electrolytes after single-electron reduction are shown

in Fig. 3g and Fig. S17, respectively. Given that solvent-separated ion pairs dominate the solvation structures of AN-based electrolyte (Fig. S15), the electrons predominantly distribute on AN solvent (Li^+-FSI^--4AN, Fig. S17). On the contrary, FAN-based electrolyte with larger contact ion pair and aggregate modes induces electrons to tilt on both FAN and FSI^-, leading to the breakage of C-F and S-F, respectively. Moreover, the reductive decomposition of FAN solvents (Li^+-FSI^--4FAN) also generate a large amount of LiF species, which favor the interphase chemistries.

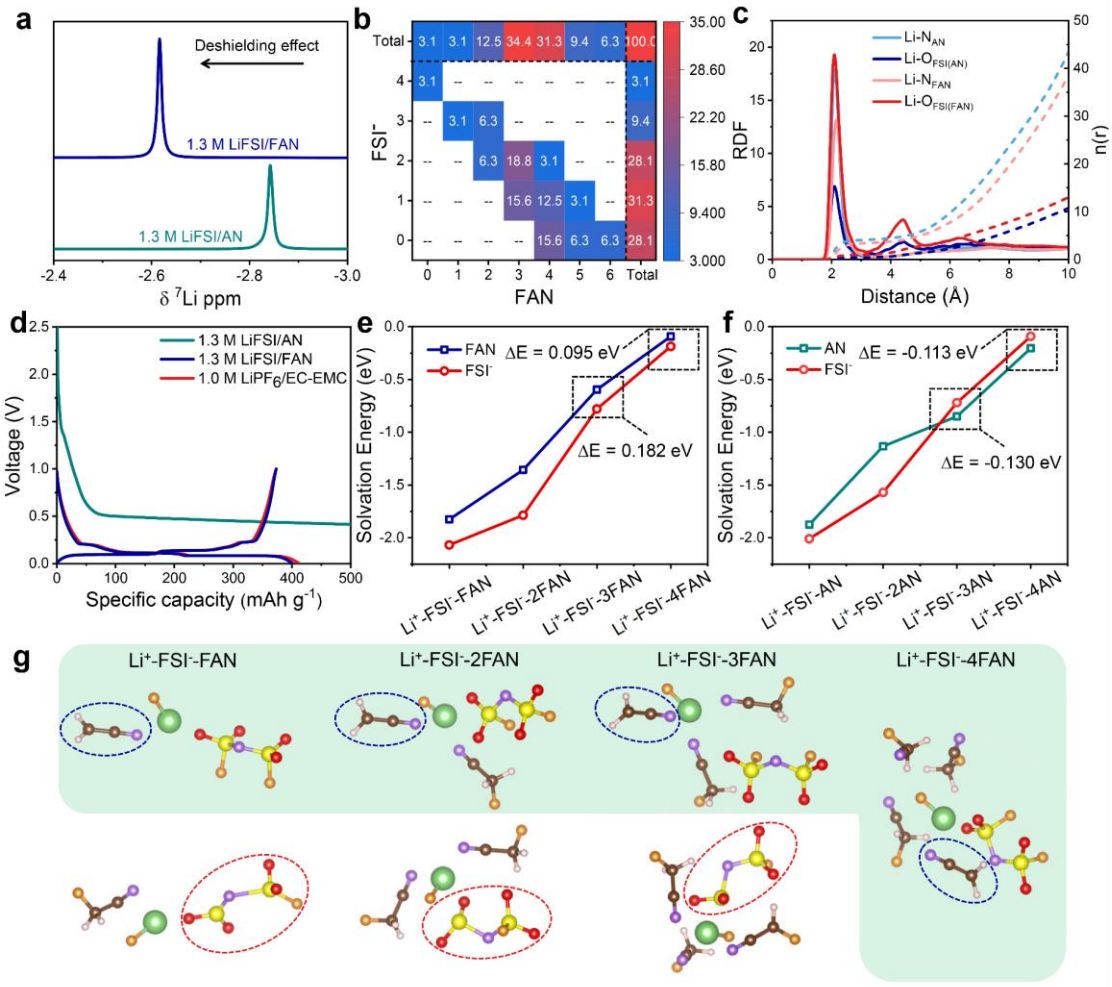

Fig. 3 | Solvation structure and lithium intercalation behavior of FAN-based electrolyte. a, ^{7}Li NMR spectra of different electrolytes. **b**, Hotmap of Li^+ solvation sheath in FAN-based electrolyte. **c**, Radial distribution function (RDF) and coordination numbers n(r) of Li-O and Li-N pairs calculated from MD simulation trajectories in AN-based and FAN-based electrolytes. **d**, Charge-discharge curves of three electrode

Li||graphite cells with different electrolytes at 1st cycle of 0.1 C. **e**,**f**, Solvation energy of solvent molecules and FSI^- with Li^+ in (**e**) FAN-based and (**f**) AN-based electrolytes. **g**, Optimized structures of FAN-based solvation complexes after single-electron reduction. The reduced solvent and anion are highlighted with navy blue and red dotted circles, respectively.

Electrochemical performances at extreme conditions

To eliminate the adverse effect of Li metal polarization on the electrochemical performance, the rate performances of cells with different electrolytes were tested using three-electrode Li||graphite cells[45]. Both FAN and EC/EMC-based electrolytes enable similar specific capacities of nearly 380.0 mAh g^{-1} at 0.1 C (Fig. S18). However, the three-electrode Li||graphite cell using FAN-based electrolyte retains much higher capacities of 369.5 mAh g^{-1}, 362.0 mAh g^{-1}, 348.5 mAh g^{-1}, 326.7 mAh g^{-1} and 299.1 mAh g^{-1} (capacity retention of 85%) at rates of 1 C, 5 C, 10 C, 15 C and 20 C, respectively. In contrast, the three-electrode Li||graphite cell with EC/EMC-based electrolyte keeps only 72.9 mAh g^{-1} (capacity retention of 19%) at 20 C. Moreover, Li||graphite cell using FAN-based electrolyte maintains an excellent capacity retention of 90% after 1000 cycles with an average Coulombic efficiency (CE) of 99.98% at 10 C, whereas the cell with traditional EC-based electrolyte keeps only 34% with an average CE of 99.90% (Fig. S18d). The impedances and overpotentials of the cells with FAN-based electrolyte are notably lower than those with EC/EMC-based electrolyte at all rates (Fig. S19, S20 and Table S4), confirming the low-resistance SEI and fast ion transport in FAN-based electrolyte. Remarkably, the FAN-based electrolyte with low resistance enables graphite||NMC811 full cells to operate effectively under extreme conditions (high voltage, high rate, and wide temperature range) without Al current

collector corrosion (Fig. S21). In Fig. 4a, graphite||NMC811 full cell with FAN-based electrolyte yields a capacity of 177.8 mAh g^{-1}, nearly 2.3 times larger than that of EC/EMC-based electrolyte (76.4 mAh g^{-1}) at 6 C. Meanwhile, graphite||NMC811 full cell with FAN-based electrolyte shows unprecedented capacity retention of 80% over 3000 cycles at 6 C with an average CE of 99.97%, which represents the lowest capacity loss reported to date for graphite||NMC811 cells at such high charge/discharge rate. Nitriles have been widely used as an effective additive for high-voltage cathodes[46,47], the FAN, as the fluorinated nitrile, exhibits even better anodic stability (Fig. S22). The 4.5 V graphite||NMC811 cell with high loading of 2 mAh cm^{-2} delivers a highly reversible capacity of 173.9 mAh g^{-1} at 4 C in FAN-based electrolyte, while that of EC/EMC-based electrolyte only remains 28.3 mAh g^{-1} (Fig. S23).

Benefitting from the unique ligand channel facilitated transport mechanism with TI = ~0.5 in the wide temperature (Fig. S24-26), FAN-based electrolyte supports high reversibility of graphite||NMC811 full cell in the whole temperature ranging from -80 °C to +60 °C (Fig. 4c and 4d). While for EC/EMC-based electrolytes, the value of TI sharply decreases from 0.3 (25 °C) to 0.04 (-20 °C) (Fig. S26a), indicating sluggish ion transport, particularly at low temperatures. At room temperature, the reversible capacities of graphite||NMC811 cells with FAN-based and EC/EMC-based electrolytes are 215.7 mAh g^{-1} and 206.5 mAh g^{-1} at 0.1 C, respectively. However, the capacity of graphite||NMC811 with EC/EMC-based electrolyte suffers from rapid capacity decay within five cycles at 60 °C due to the instability of SEI/CEI at elevated temperatures[48] (Fig. 4c and Fig. S27). In contrast, the graphite||NMC811 full cell with FAN-based

electrolyte shows a high capacity of 175.0 mAh g^{-1} at 6 C and stable cycling performance with a capacity retention of 80% after 600 cycles with an average CE of 99.95% at 60 °C (Fig. 4e and Fig. S27). To better demonstrate the superiority of our electrolyte under extreme conditions, we also compared the wide-temperature electrochemical performance of recently reported electrolytes (E1-E9) (Table S5 and Fig. S30). In Fig. 4e and Fig. S31, the graphite||NMC811 full cells with E1 and E2 exhibit an inferior high-temperature cycling performance. It is worth noting that low-temperature charging is particularly challenging for graphite-based LIBs as previous studies mainly focused on discharging. This is due to the high interfacial resistance and the low Li-intercalation potential of the graphite, which makes graphite lithiation difficult at low temperatures[12,26,49]. In current work, the FAN-based electrolyte exhibits excellent performance for both charging and discharging at ultra-low temperatures. The graphite||NMC811 full cell using this electrolyte demonstrate high retention of their room-temperature capacity, with 76% (164.8 mAh g^{-1}), 68% (147.1 mAh g^{-1}), 63% (135.0 mAh g^{-1}), 57% (123.1 mAh g^{-1}), and 51% (109.7 mAh g^{-1}) retention at -35 °C, -45 °C, -60 °C, -70 °C, and -80 °C, respectively. Moreover, the graphite||NMC811 cell with FAN-based electrolyte displays an extremely stable and reversible capacity over 350 cycles (capacity retention: 96%, average CE of 99.95%)) at -35 °C (Fig. 4f). Even at -60 °C, the cell still maintains a capacity retention of 80% with an average CE of 99.93% after 350 cycles without Li plating (Fig. S28), whereas the cell employing EC/EMC-based electrolyte cannot provide any capacity at temperatures below -35 °C (Fig. 4f and Fig. S29). Unfortunately, the graphite||NMC811 cell with E3 retains only

49% capacity retention after 350 cycles at -35 °C, and a low capacity of 17.9 mAh g^{-1} after 20 cycles at -60 °C (Fig. S32). As the scaled-up cell format, 1.2 Ah graphite||NMC811 pouch cells (area capacity of cathode/anode: 2.85 mAh cm^{-2}/3.13 mAh cm^{-2}) with lean electrolyte (3 g Ah^{-1}) were further evaluated (Fig. 4g). Impressively, the 1.2 Ah pouch cell with FAN-based electrolyte can deliver a reversible capacity of about 0.73 Ah, which was charged and discharged at -50 °C, maintaining high reversibility without any capacity decay over 150 cycles, while that with E3-E9 cannot show any capacity. When the temperature drops to -65 °C, -70 °C and -80 °C, the graphite||NMC811 pouch cells with FAN-based electrolyte still exhibit reversible capacity of 0.62 Ah, 0.55 Ah and 0.45 Ah, respectively (Fig. S33). These findings indicate a significant advancement in the rechargeability of graphite anodes under ultra-low temperatures and ultra-high rates, thus validating the electrolyte design principles for fast Li-ion chemistries.

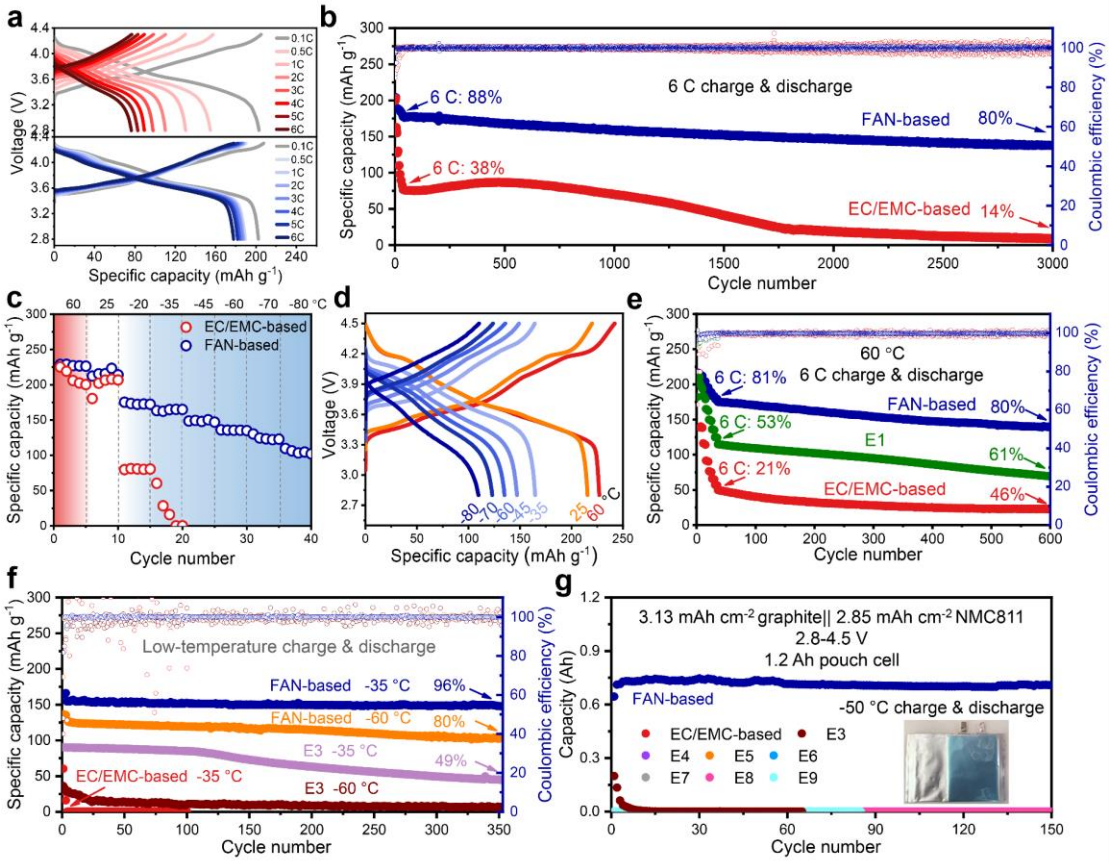

Fig. 4 | Electrochemical performances of FAN-based electrolyte at extreme conditions. a, Charge-discharge curves of graphite||NMC811 cells at different rates for EC/EMC-based (top) and FAN-based electrolyte (bottom) at 25 °C. **b**, Cycling performance of graphite||NMC811 cells with different electrolytes in the range of 2.8-4.3 V at 25 °C (0.1 C, 0.5 C, 1 C, 2 C, 3 C, 4 C, 5 C, 6 C each cycled for 5 cycles, and then 6 C for long cycling). **c,** Specific capacities and (**d**) Charge-discharge curves of graphite||NMC811 cells with FAN-based electrolyte in the range of 2.8-4.5 V at different temperatures. **e**, Cycling performance of graphite||NMC811 cells with different electrolytes in the range of 2.8-4.3 V at 60 °C (0.1 C, 0.5 C, 1 C, 2 C, 3 C, 4 C, 5 C, 6 C each cycled for 5 cycles, and then 6 C for long cycling). **f**, Cycling performance of graphite||NMC811 cells with different electrolytes in the range of 2.8-4.5 V at -35 °C and -60 °C. **g**, Cycling performance of graphite||NMC811 pouch cells with different electrolytes in the range of 2.8-4.5 V at -50 °C. The electrolytes of E1-E9 are listed in Table S5.

Chemistry at the interphase

The SEI formed on graphite anode in 1.3 M LiFSI/FAN electrolyte is designed to be rich in LiF-Li_xN, as confirmed by high-resolution transmission electron microscopy (HRTEM), soft X-ray absolution spectroscopy (XAS) and theoretical calculations.

During the initial decomposition reactions of FAN-based electrolyte (Fig. 5a-c), the FSI^- anions form anion-derived SEI by gradually accepting electrons. Simultaneously, FAN solvents are prone to being reduced with the lowest reaction energy of -4.73 eV, resulting in the formation of LiF-Li_xN-rich SEI. The value of Mayer Bond order (MBO) of C≡N is reduced from 3.06 to 2.49 and 2.08, suggesting substantial novel C=N moieties are generated over cycling. These findings are consistent with the in-depth X-ray photoelectron spectroscopy (XPS) results (Fig. S34-S36). On the contrary, EC/EMC-based electrolyte tends to produce considerable organic Li-O species on graphite anode during the initial decomposition reactions (Fig. S37 and S38), which leads to sluggish Li^+ transport kinetics. As shown in Fig. 5d and 5e, the SEI formed by the FAN-based electrolyte is more uniform and thinner (2.7 nm) compared to the SEI formed by EC/EMC-based electrolyte (11.4 nm). Such homogenous interphase films are also detected on NMC811 cycled in FAN-based electrolyte (Fig. S39). Notably, XAS with total electron yield (TEY, surface sensitive, ~10 nm) mode and fluorescence yield (FY, bulk sensitive, ~100 nm) mode are powerful techniques for probing deep structure analysis and providing statistical information of interfacial and bulk species on electrode. The peaks observed at around 288.5 eV (C=O, C K-edge, Fig. 5f) and 534.0 eV (C=O, O K-edge) are attributed to carbonyl groups and their presence in the pristine anode is caused by Li_2CO_3, a native passivation film commonly found on graphite surfaces. After cycling in FAN-based electrolyte, these peak intensities are greatly reduced due to the formation of SEI layer. In the case of EC/EMC-based electrolyte, these peaks are well maintained after cycling due to the generation of new

carbonyl-containing species such as lithium alkylcarbonates resulting from the decomposition of EC/EMC solvents. The appearance of new species of C=N (286.8 eV, C K-edge and 399.8 eV, N K-edge) and LiF (692.2 eV, F K-edge) on graphite anode cycled in FAN-based electrolyte indicates the decomposition of FAN solvent, which is consistent with AIMD results (Fig. 5a-c and Fig. S38). Meanwhile, the C=N and LiF species are also observed in the bulk structures of graphite anode (FY mode of XAS as shown in Fig. S40), suggesting that the initial decomposition of FSI^- anions and FAN solvents, followed by further decomposition of FAN solvent, helps to improve the stability of bulk graphite anode. This effective and low-resistance SEI formation mechanism promotes the achievement of ultra-fast LIBs under extreme conditions.

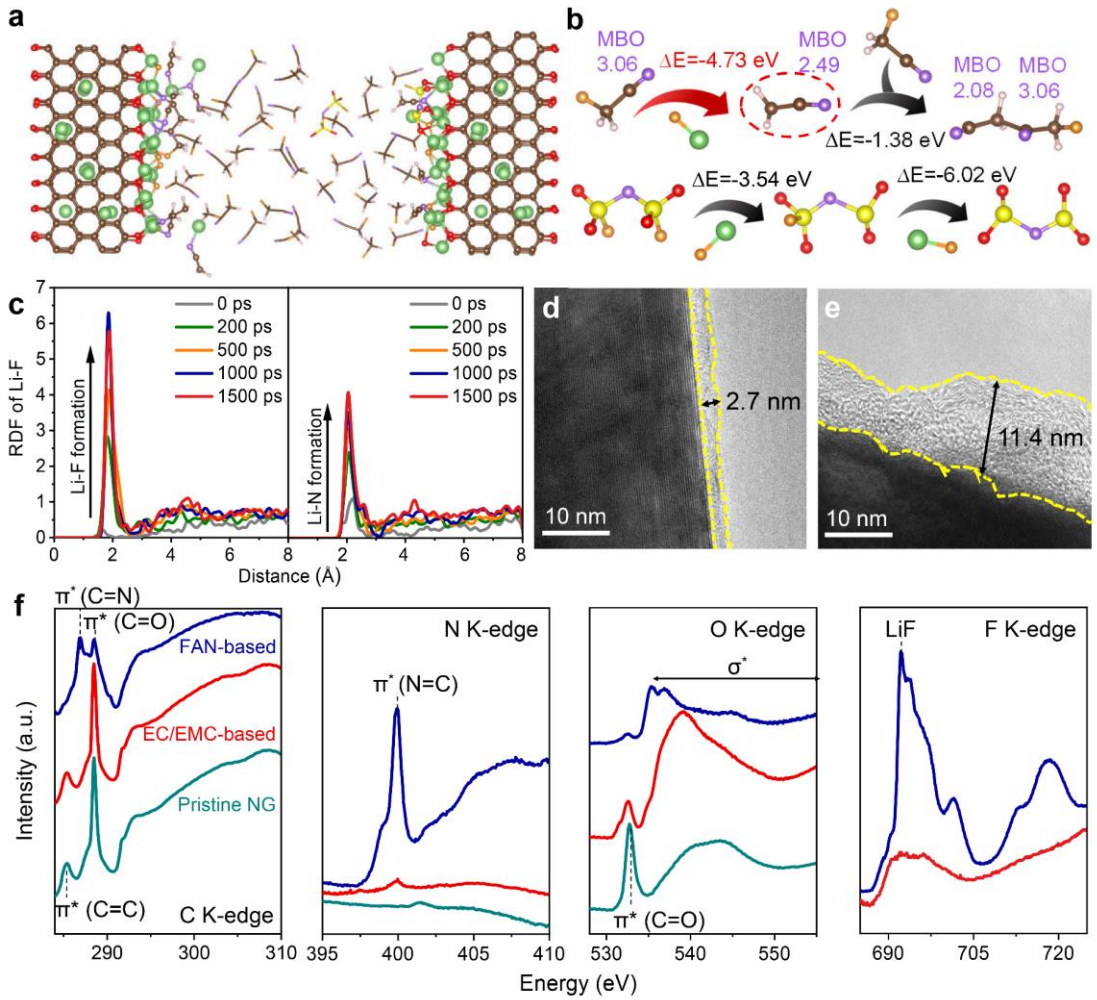

Fig. 5 | FAN-based electrolyte/electrode interphase analysis. a, The initial decomposition reaction of FAN-based electrolyte on the anode interphase calculated by AIMD. **b**, Energetics for multistep decomposition pathways of FAN and anion, Mayer Bond order (MBO) of CN bonds (the red circle represents the most decomposed product). **c**, RDF curves of Li-F (left) and Li-N (right). **d**,**e**, HRTEM images of graphite anodes recovered from graphite||NMC811 cells using (**d**) FAN-based and (**e**) EC/EMC-based electrolyte after 100 cycles, respectively. **f**, Characterization of pristine and cycled graphite anodes (after 100 cycles) by the total electron yield (TEY) mode of soft XAS: C K-edge, N K-edge, O K-edge and F K-edge. The probing depth of soft XAS in TEY is around 10 nm.

Conclusion

In summary, the ideal electrolyte requires contradictory properties of high salt dissociation but low Li^+ transport energy barrier and high ionic conductivity but inorganic-rich interphase, which is never achieved simultaneously. Taking advantages

of the ligand channel facilitated mechanism, we designed a unique electrolyte (1.3 M LiFSI/FAN) with small solvation sheath and fast solvation/desolvation capability. The FAN-based electrolyte demonstrates an ultra-high ionic conductivity of 40.3 mS cm^{-1} at 25 °C and 11.9 mS cm^{-1} at -70 °C. It also realizes fast charge transfer kinetics and promotes the formation of conductive LiF-Li_xN-rich SEI, which overcomes the sluggish kinetics of graphite during ultra-fast charging and ultra-low temperature conditions. The graphite||NMC811 full cell with FAN-based electrolyte exhibits >3000 cycles life at 6 C and delivers a high reversible capacity of 109.7 mAh g^{-1} when charged and discharged at -80 °C. Practical 1.2 Ah graphite||NMC811 pouch cell (area capacity of cathode/anode: 2.85 mAh cm^{-2}/3.13 mAh cm^{-2}) using FAN-based electrolyte delivers highly reversible capacity of 0.73 Ah at -50 °C (0.62 Ah at -65 °C) with no capacity decay after 150 cycles. This work also sheds light on ion motion between vehicular and structural mechanism. The ligand channel facilitated conduction paves the way for high-energy batteries operating at extreme conditions.

Experimental Section

Preparation of electrolytes and electrodes

Battery-grade $LiPF_6$, LiFSI, LiTFSI and Py_{13}-FSI were purchased from Changde Dadu New Material Co., Ltd. EC, EMC, DMC, DME, DOL, BTFE, AN and FAN were purchased from Sigma-Aldrich. The EC/EMC-based electrolyte and FAN-based electrolyte were 1.0 M $LiPF_6$/EC-EMC (3:7, v/v) and 1.3 M LiFSI/FAN, respectively. All solvents were dried over activated molecular sieves before use. All electrolytes were prepared in an argon-filled glovebox (Mikrouna, China) with moisture and oxygen contents less than 0.1 ppm. The solid-state electrolyte $Li_{10}GeP_2S_{12}$ (LGPS) was synthesized according to previously reported procedures[50,51].

The anode slurry coated on copper foil was composed of 80 wt.% natural graphite (graphite, average diameters: 2.5 μm, Beijing Xinjincheng Science and Trade Co., Ltd.), 10 wt.% conductive carbon black (Super C45, Hefei Kejing Materials Technology Co., Ltd.), 10 wt.% PAALi (Sigma-Aldrich) and pure H_2O as solvent. The cathode slurry coated on aluminum foil was consisted of 80 wt.% NMC811 (Hefei Kejing Materials Technology Co., Ltd.), 10 wt.% conductive carbon black (Super C45, Hefei Kejing Materials Technology Co., Ltd.), 10 wt.% polyvinylidene fluoride binder (PVDF, Suzhou Zhongyan Chemical Technology Co., Ltd.) and N-methyl-2-pyrrolidinone (NMP, Suzhou Zhongyan Chemical Technology Co., Ltd.) as solvent. After solvents have been dried, the electrodes were punched into disks with diameters of 14 and 12 mm for anodes and cathodes, respectively, followed by additional vacuum drying at 100 °C overnight prior to the assembling of both half cells and full cells. The mass

loading of NMC811 and graphite for coin cells were about 5.00 mg cm^{-2} and 2.95 mg cm^{-2}, respectively. Coin cells with as-prepared electrolytes (80 μL) were assembled with NMC811 (or graphite) as working electrode and PE membrane (ND16, SK Innovation Co., Ltd.) as separator. For coin full cells, the N/P value was 1.1 (calculated according to 200 mAh g^{-1} for NMC811 and 372 mAh g^{-1} for graphite). The graphite||NMC811 pouch-type cells (1.2 Ah) (LI-FUN Technology Co., Ltd.) were injected with 3 g electrolytes before sealing. Due to incompatibility between Li metal and AN solvent, co-intercalate behavior of AN-based electrolyte was investigated by graphite||4 mAh cm^{-2} $LiFePO_4$ full cell. Viscosity of electrolytes were performed by Anton Paar MCR102e Rheometer. Different electrolytes subjected to differential scanning calorimetry (DSC) measurement was packed in a stainless-steel pan, which was then crimp-sealed in a glove box filled with argon. All of the DSC experiments were carried out at a cooling/heating rate of 5 °C min^{-1}.

Electrochemical measurements

All cells were charged and discharged both at a certain same temperature between -80 °C to 60 °C instead of previously reported room-temperature charging and low-temperature discharging protocol using a LAND battery testing system (Wuhan LAND electronics Co., Ltd.). For coin-type cells at extreme conditions, the graphite||NMC811 cells were cycled at 0.5 C for first 10 cycles at room temperature, followed by long cycling at 0.2 C at low temperatures (-35 to -60 °C, 0.1 C for -70 and -80 °C). For pouch-type cells at extreme conditions, the graphite||NMC811 cells were cycled at 0.2 C for first 10 cycles at room temperature, followed by long cycling at 0.1 C at low

temperatures (-50 °C and -65 °C). In galvanostatic intermittent titration technique (GITT) measurements, the Li||graphite cells were cycled at a rate of 10 C and 3 h rest time (after 60 cycles at 10 C charge and discharge). Two plate electrodes were inserted into electrolytes (6 mL) to measure ionic conductivities of the electrolytes by an AC impedance analysis using an Ivium-n-stat with an AC voltage amplitude of 10 mV over the frequency range from 1 Hz to 1 MHz at various temperatures and concentrations. The electrochemical impedance spectroscopy (EIS) spectra of coin cells at fully discharged state were performed by an electrochemical workstation (lithium-n-state, lvium Technologies BV Co., Ltd.) over frequencies from 10 kHz to 10 mHz with a voltage amplitude of 10 mV.

Characterization

The solvation structures of different electrolytes were measured by ^{7}Li and ^{19}F nuclear magnetic resonance spectroscopy (600 MHz NMR, AgilentDD2 600). The cathodes and anodes were disassembled from graphite||NMC811 full cells cycled 100 cycles and rinsed with anhydrous DMC three times to remove the residuals (inside the glovebox), followed by characterizations of Scanning electron microscope (SEM, SU-70, Hitachi Ltd.), Transmission electron microscopy (TEM, Tecnai G2 F20), X-ray photoelectron spectroscopy (XPS, Escalab 250Xi, Thermo Fisher Scientific). Samples were transferred directly to the XPS sample chamber to avoid interference from the external rings. X-ray absorption spectroscopy (XAS) of anodes were performed at beamline 23-ID-2 of National Synchrotron Light Source (NSLS) II at Brookhaven National Laboratory. The soft XAS measurements for obtaining interspatial and bulk information

were conducted in both total electron yield and fluorescence yield modes at the IOS beamline of NSLS II. The collected XAS data were analyzed using the ATHENA software package.

Quantum chemistry calculations

All quantum chemistry calculations were performed using the Gaussian 16 software. The M06-2X functional was used as it was shown to accurately describe long-range van der Waals interaction of intermolecular interactions. The tribble-zeta basis set def2-TZVP was used for structure optimization as well as the energy calculation. All the optimized structures were confirmed as potential minima, with no frequency modes with imaginary eigenvalues, through frequency analyses following geometry optimizations. The SMD implicit solvation model with AN (ε = 35.688) was used to represent different electrolyte environments not explicitly included in quantum chemistry calculations.

The solvation energy of the *n* th solvent (AN and FAN) is defined as the energy difference between (LiFSI: *n* solvent) and [LiFSI: (*n*-1) solvent] and solvent. While the solvation energy of FSI^- with the (Li^+: *n* solvent) is defined as the energy difference between (LiFSI: *n* solvent) and (Li^+: *n* solvent) and FSI^-. The Mayer bond order was calculated by using the Multiwfn 3.8 program.

Classical molecular dynamics simulations

Classical molecular dynamics (cMD) simulations were performed in LAMMPS using the all-atom optimized potentials for liquid simulations (OPLS-AA) force-field with the Li^+, PF_6^- and FSI^- anions description from previous publications. The electrolyte

systems were set up initially with the salt and solvent molecules distributed in the simulation boxes using Moltemplate (http://www.moltemplate.org/). For each system, an initial energy minimization at 0 K (energy and force tolerances of 10^{-5}) was performed to obtain the ground-state structure. After this, the system was slowly heated from 0 K to room temperature (298 K) at a constant volume over 0.2 ns using a Langevin thermostat, with a damping parameter of 100 ps. The system was equilibrated in the constant temperature (298 K), and constant pressure (1 bar) (NPT ensemble) for 5 ns. For production runs, a series of 50-ns simulations at 300 K were carried out in the NVT ensemble using a Nosé-Hoover thermostat with a coupling constant of 0.1 ps. Radial distribution functions were obtained using the Visual Molecular Dynamics (VMD) software. Snapshots of the most probable solvation sheaths were also sampled from the simulation trajectory using VESTA.

The ionic transport behavior of given electrolyte was evaluated via equilibrium classical MD simulations. The model with the scaled charges by 0.75 for charged ions was utilized to account for electronic screening and obtain converged conductivity and ionicity values. The transport coefficients (F_{ij}) and ionic conductivity (σ) calculated using the equation (5) and (6).

$$F_{ij} = \frac{1}{6}\lim_{t\to\infty}\frac{d}{dt}\langle\frac{1}{n_i}\sum_{\alpha}^{N}\left[r_{i,\alpha}(t) - r_{i,\alpha}(0)\right]\cdot\frac{1}{n_j}\sum_{\beta}^{N}\left[r_{i,\beta}(t) - r_{i,\beta}(0)\right]\rangle \quad (5)$$

$$\sigma = \frac{e^2}{Vk_BT}\sum_{i,j} z_i z_j n_i n_j F_{ij} \quad (6)$$

where e is the electron charge, V is the volume of the simulation box, k_B is Boltzmann's constant, T is the temperature. i and j represent species and n_i (n_j) is the number of

particles of species *i* (*j*). $\boldsymbol{r}_{i,\alpha}$ is the displacement vectors for the motion of αth particle of species *i* relative to the center-of-mass position of the entire system[52,53].

Ab Initio molecular dynamics calculations

AIMD simulations were performed using CP2K. We used the PBE exchange-correlation functional, a GGA functional, and the double-zeta valence polarized basis set and Goedecker-Teter-Hutter pseudopotentials. The efficient solution of the Poisson equation within the PBC is obtained in the reciprocal space by the expansion of the electronic density into a plane-wave basis set truncated at the energy cutoff of 400 Ry. The dispersion correction was applied in all calculations with the Grimme D3 method. Because of the large size of the cells, only the Gamma point in the reciprocal space was used in our calculations. AIMD simulations were performed at 300 K with NVT ensembles and a timestep of 1.0 fs. Stochastic velocity rescaling thermostat was used to control the temperature in AIMD simulations.

For simulations of Li^+ hopping transfer behavior in bulk solvent, various solvent molecules with two Li^+ complexes were employed in a periodic cubic box (column is calculated based on density). A 20-ps simulation was performed to sample Li^+ transfer in bulk solvent. We extract the free energy of Li^+ hopping as:

$$\Delta E_{trans} = -k_B T \ln P \tag{7}$$

where P is the probability as a function of Li-O (N) coordinate, T is temperature, and k_B is the Boltzmann constant.

The anode is comprised of three layers of fully discharged graphite (LiC_6) with an

arm-chair edge. Carbon arm-chair edges were functionalized with all oxygens. Two electrolyte systems, 1.3 M LiFSI/FAN (2 LiFSI and 40 FAN molecules) and 1.0 M $LiPF_6$/EC-EMC (2 $LiPF_6$, 8 EC, and 12 EMC molecules) were evaluated. Initial geometries of the electrolyte were created with PACKMOL and then quenched using density functional forces. AIMD simulations were then performed at an elevated temperature of 350 K using a Nose thermostat to allow fast equilibration. At least 5 ps of dynamic simulations were performed for each system studied.

References and Notes

1. Tarascon, J.-M. & Armand, M. Issues and challenges facing rechargeable lithium batteries. *Nature* **414**, 359-367 (2001).
2. Dunn, B., Kamath, H. & Tarascon, J.-M. Electrical energy storage for the grid: a battery of choices. *Science* **334**, 928-935 (2011).
3. Rodrigues, M.-T. F. et al. A materials perspective on Li-ion batteries at extreme temperatures. *Nat. Energy* **2**, 17108 (2017).
4. Liu, Y., Zhu, Y. & Cui, Y. Challenges and opportunities towards fast-charging battery materials. *Nat. Energy* **4**, 540-550 (2019).
5. Fan, X. & Wang, C. High-voltage liquid electrolytes for Li batteries: progress and perspectives. *Chem. Soc. Rev.* **50**, 10486-10566 (2021).
6. Yao, N., Chen, X., Fu, Z. H. & Zhang, Q. Applying classical, *ab initio*, and machine-learning molecular dynamics simulations to the liquid electrolyte for rechargeable batteries. *Chem. Rev.* **122**, 10970-11021 (2022).
7. Xu, K. Nonaqueous liquid electrolytes for lithium-based rechargeable batteries. *Chem. Rev.* **104**, 4303−4417 (2004).
8. Gupta, A. & Manthiram, A. Designing advanced lithium-based batteries for low-temperature conditions. *Adv. Energy Mater.* **10**, 2001972 (2020).
9. Zhang, S., Xu, K. & Jow, T. The low temperature performance of Li-ion batteries. *J. Power Sources* **115**, 137-140 (2003).
10. Yu, Z. *et al.* Molecular design for electrolyte solvents enabling energy-dense and long-cycling lithium metal batteries. *Nat. Energy* **5**, 526-533 (2020).
11. Huang, Y. *et al.* Eco-friendly electrolytes via a robust bond design for high-

energy Li metal batteries. *Energy Environ. Sci.* **15**, 4349-4361 (2022).

12. Fan, X. *et al.* All-temperature batteries enabled by fluorinated electrolytes with non-polar solvents. *Nat. Energy* **4**, 882-890 (2019).

13. Yao, Y. *et al.* Regulating interfacial chemistry in lithium-ion batteries by a weakly solvating electrolyte. *Angew. Chem. Int. Ed.* **60**, 4090-4097 (2021).

14. Jiang, L. *et al.* Inhibiting solvent co-intercalation in a graphite anode by a localized high-concentration electrolyte in fast-charging batteries. *Angew. Chem. Int. Ed.* **60**, 3402-3406 (2021).

15. Self, J., Fong, K. D. & Persson, K. A. Transport in superconcentrated $LiPF_6$ and $LiBF_4$/propylene carbonate electrolytes. *ACS Energy Lett.* **4**, 2843-2849 (2019).

16. Siegel, D. J., Nazar, L., Chiang, Y.-M., Fang, C. & Balsara, N. P. Establishing a unified framework for ion solvation and transport in liquid and solid electrolytes. *Trends Chem.* **3**, 807-818 (2021).

17. He, X., Zhu, Y. & Mo, Y. Origin of fast ion diffusion in super-ionic conductors. *Nat Commun* **8**, 15893 (2017).

18. Tang, Z. K., Tse, J. S. & Liu, L. M. Unusual Li-ion transfer mechanism in liquid electrolytes: a first-principles study. *J. Phys. Chem. Lett.* **7**, 4795-4801 (2016).

19. Zheng, X. *et al.* Critical effects of electrolyte recipes for Li and Na metal batteries. *Chem* **7**, 2312-2346 (2021).

20. Aihara, Y., Sugimoto, K., Price, W. S. & Hayamizu, K. Ionic conduction and self-diffusion near infinitesimal concentration in lithium salt-organic solvent electrolytes. *J. Chem. Phys.* **113**, 1981-1991 (2000).

21. Borodin, O. & Smith, G. D. Li^+ transport mechanism in oligo(ethylene oxide)s compared to carbonates. *J. Solut. Chem.* **36**, 803-813 (2007).

22. Wang, J. *et al.* Fire-extinguishing organic electrolytes for safe batteries. *Nat. Energy* **3**, 22-29 (2017).

23. Yamada, Y., Wang, J., Ko, S., Watanabe, E. & Yamada, A. Advances and issues in developing salt-concentrated battery electrolytes. *Nat. Energy* **4**, 269-280 (2019).

24. Borodin, O. *et al.* Liquid structure with nano-heterogeneity promotes cationic transport in concentrated electrolytes. *ACS Nano* **11**, 10462-10471 (2017).

25. Okoshi, M., Chou, C. P. & Nakai, H. Theoretical analysis of carrier ion diffusion in superconcentrated electrolyte solutions for sodium-ion batteries. *J. Phys. Chem. B* **122**, 2600-2609 (2018).

26. Xu, J. *et al.* Electrolyte design for Li-ion batteries under extreme operating conditions. *Nature* **614**, 694-700 (2023).

27. Rustomji, C. S. *et al.* Liquefied gas electrolytes for electrochemical energy storage devices. *Science* **356**, 1351 (2017).

28. Yang, Y. *et al.* Liquefied gas electrolytes for wide-temperature lithium metal batteries. *Energy Environ. Sci.* **13**, 2209-2219 (2020).

29. Dong, X., Guo, Z., Guo, Z., Wang, Y. & Xia, Y. Organic Batteries Operated at −70°C. *Joule* **2**, 902-913 (2018).

30. Borodin, O., Self, J., Persson, K. A., Wang, C. & Xu, K. Uncharted waters: super-concentrated electrolytes. *Joule* **4**, 69-100 (2020).

31. Yin, Y. et al. Fire-extinguishing, recyclable liquefied gas electrolytes for temperature-resilient lithium-metal batteries. *Nat. Energy* **7**, 548-559 (2022).

32. Sun, C. *et al.* 50C fast-charge Li-ion batteries using a graphite anode. *Adv. Mater.* **34**, 2206020 (2022).

33. Ren, X. *et al.* Role of inner solvation sheath within salt-solvent complexes in tailoring electrode/electrolyte interphases for lithium metal batteries. *Proc. Natl. Acad. Sci. U. S. A.* **117**, 28603-28613 (2020).

34. Suo, L. *et al.* "Water-in-salt" electrolyte enables high-voltage aqueous lithium-ion chemistries. *Science* **350**, 938-943 (2015).

35. Ue, M. & Mori, S. Mobility and ionic association of lithium salts in a propylene carbonate-ethyl methyl carbonate mixed solvent. *J. Electrochem. Soc.* **142**, 2577-2581 (1995).

36. Ren, Y. *et al.* Oxide electrolytes for lithium batteries. *J. Am. Ceram. Soc.* **98**, 3603–3623 (2015).

37. Xing, L. *et al.* Deciphering the ethylene carbonate-propylene carbonate mystery in Li-ion batteries. *Acc. Chem. Res.* **51**, 282-289 (2018).

38. Chao, D. *et al.* Roadmap for advanced aqueous batteries: From design of materials to applications. *Sci. Adv.* **6**, 1-19 (2020).

39. Wang, Y., Yi, J. & Xia, Y. Recent progress in aqueous lithium-ion batteries. *Adv. Energy Mater.* **2**, 830-840 (2012).

40. Rupich, M. W., Pitts, t. & Abraham, K. M. Characterization of reactions and products of the discharge and forced overdischarge of Li / SO_2 Cells. *J.*

Electrochem. Soc. **129**, 1857-1861 (1982).

41. Yamada, Y. *et al.* Unusual stability of acetonitrile-based superconcentrated electrolytes for fast-charging lithium-ion batteries. *J. Am. Chem. Soc.* **136**, 5039-5046 (2014).

42. Nan, B. *et al.* Enhancing Li^+ transport in NMC811||graphite lithium-ion batteries at low temperatures by using low-polarity-solvent electrolytes. *Angew. Chem. Int. Ed.* **61**, e202205967 (2022).

43. Seo, D. M. *et al.* Electrolyte solvation and ionic association III. acetonitrile-lithium salt mixtures–transport properties. *J. Electrochem. Soc.* **160**, A1061-A1070 (2013).

44. Kreuer, K.-D., Rabenau, A. & Weppner, W. Vehicle Mechanism, a new model for the interpretation of the conductivity of fast proton conductors. *Angew. Chem. Int. Ed. Engl.* **21**, 208-209 (1982).

45. Yao, Y. *et al.* Unlocking charge transfer limitations for extreme fast charging of Li-ion batteries. *Angew. Chem. Int. Ed.* **62**, e202214828 (2023).

46. Yang, X. *et al.* Enabling stable high-voltage $LiCoO_2$ operation by using synergetic interfacial modification strategy. *Adv. Funct. Mater.* **30**, 2004664 (2020).

47. Zhi, H., Xing, L., Zheng, X., Xu, K. & Li, W. Understanding how nitriles stabilize electrolyte/electrode interface at high voltage. *J. Phys. Chem. Lett*. **8**, 6048-6052 (2017).

48. Lu, D. *et al.* A self-purifying electrolyte enables high energy Li ion batteries.

Energy Environ. Sci. **15**, 3331-3342 (2022).

49. Gao, Y. *et al.* Low-temperature and high-rate-charging lithium metal batteries enabled by an electrochemically active monolayer-regulated interface. *Nat. Energy* **5**, 534-542 (2020).

50. Kamaya, N. *et al.* A lithium superionic conductor. *Nat. Mater.* **10**, 682-686 (2011).

51. Hayashi, A., Hama, S., Morimoto, H., Tatsumisago, M. & Minami, T. Preparation of Li_2S-P_2S_5 amorphous solid electrolytes by mechanical milling. *J. Am. Ceram. Soc.* **84**, 477-479 (2001).

52. Fang, C., Mistry, A., Srinivasan, V., Balsara, N. P. & Wang, R. Elucidating the molecular origins of the transference number in battery electrolytes using computer simulations. *JACS Au* **3**, 306-315 (2023).

53. Fong, K. D., Self, J., McCloskey, B. D. & Persson, K. A. Onsager transport coefficients and transference numbers in polyelectrolyte solutions and polymerized ionic liquids. *Macromolecules* **53**, 9503-9512 (2020).

Acknowledgments: This work is supported by the National Natural Science Foundation of China (22161142017, 22072134 and U21A2081), Natural Science Foundation of Zhejiang Province (LR23B030002 and LZ21B030002), the Fundamental Research Funds for the Central Universities (2021FZZX001-09), and "Hundred Talents Program" of Zhejiang University. M. R. and E. H. are supported by the Assistant Secretary for Energy Efficiency and Renewable Energy (EERE), Vehicle

Technology Office (VTO) of the US Department of Energy (DOE) through the Advanced Battery Materials Research (BMR) Program under contract no. DE-SC0012704. This research used beamlines 23-ID-2 of the National Synchrotron Light Source II, a US DOE Office of Science user facility operated for the DOE Office of Science by Brookhaven National Laboratory under contract number DE-SC0012704.

Author contributions: D. L. R. L. and X. F. conceived the idea and designed the experiments. D. L., L. L., S. Y., Y. H., C. S., S. Z., H. Z. and J. Z. conducted the electrochemical experiments and characterizations with the assistance of X. X., L. F., L. C. and X. F.. R. M. performed XAS under E. H.'s guidance. R. L. provided the therotical calculations. D. L., T. D., E. H., C. W., and X. F. prepared the manuscript with the input of all the co-authors. All authors endorsed the final version of the manuscript.

Competing interests: There are no conflicts to declare.

Supplementary Materials:

Supplementary Text

Figures. S1 to S40

Tables S1 to S5

Supplementary references